Eastern Mediterranean Sea circulation inferred from the conditions of S1 sapropel deposition

Kazuyo Tachikawa[1], Laurence Vidal[1], Marine Cornuault[1], Marta Garcia[1], Audrey Pothin[2], Corinne Sonzogni[1], Edouard Bard[1], Guillemette Menot[1], and Marie Revel[2]

1: Aix-Marseille Université, CNRS, IRD, Collège de France, CEREGE UM34, 13545 Aix en Provence, France (kazuyo@cerege.fr)

2: Geoazur, UMR 7329, 06560 Valbonne-Sophia Antipolis, France

Abstract

Holocene Eastern Mediterranean Sea sediments contain an organic-rich sapropel S1 layer that was formed in oxygen-depleted waters. The spatial distribution of this layer revealed that during S1 deposition deep waters were anoxic below 1,800 m in water depth. However, whether this boundary permanently existed from early to mid-Holocene has not been examined yet. To answer this question, a multi-proxy approach was applied to a core retrieved close to the 1,800 m boundary (at 1,780 m). We measured the bulk sediment elemental composition, the stable isotopic composition of the planktonic foraminifer *Globigerinoides ruber,* and the abundance of benthic foraminifera since the last deglaciation. The result indicates that authigenic U and Mo accumulation began around 13-12 cal ka BP, in concert with surface water freshening estimated from the *G. ruber* $\delta^{18}O$ record. The onset of bottom/pore water oxygen depletion occurred prior to S1 deposition inferred from barium enrichment. In the middle of the S1 deposition period reduced authigenic V, Fe and As contents and Br/Cl ratio indicated short-term bottom water re-oxygenation. A sharp Mn peak and maximal abundance for benthic foraminifera marked a total recovery for circulation at

approximately 7 cal ka B.P. Based on our results and existing data, we suggest that S1 formation within the upper 1,780 m of the Eastern Mediterranean Sea was preconditioned by reduced ventilation, resulting from excess fresh water inputs due to insolation changes under deglacial conditions, that initiated between 15 and 12 ka within the upper 1,780 m. Short-term re-oxygenation in the Levantine Basin is estimated to have affected bottom water at least as deep as 1,780 m in response to cooling and/or reduction of fresh water inputs. We tentatively propose that complete ventilation recovery at the S1 termination was depth-dependent with earlier oxygenation within the upper 1,780 m. Our results provide new constraints of vertical water column structure in the eastern Mediterranean Sea since the last deglaciation.

1. Introduction

The Mediterranean Sea is located in a transition zone between subpolar depression and subtropical high pressure and is known to be sensitive to on-going and past climate change (Bethoux and Gentili, 1999; Roether et al., 1996). Holocene sediments obtained from the eastern Mediterranean Sea often contain the most recent organic-rich sapropel deposit, S1 (10.8 ± 0.4 to 6.1 ± 0.5 cal ka B.P., De Lange et al., 2008), that formed due to a drastic decrease in labile organic matter decomposition (Moodley et al., 2005). Reduced oxygen supply to bottom waters has been suggested to be a precondition for sapropel formation although increased biological productivity further promoted S1 deposition (Bianchi et al., 2006; Myers et al., 1998; Rohling, 1994; Stratford et al., 2000).

Surface water density decreases due to excess fresh water inputs have played a pivotal role in reducing Mediterranean Sea thermohaline circulation during sapropel formation (Myers et al., 1998; Rohling, 1994; Stratford et al., 2000). By reinforcing Nile River discharge toward the Levantine Sea (Emeis et al., 2003; Kallel et al., 1997; Revel et al., 2010; Rohling, 1994; Rossignol-Strick et al., 1982), high summer insolation at minimum precession

is known to have had a fundamental impact (Kutzbach et al., 2014; Rohling, 1994 and references therein; Ziegler et al., 2010). In parallel, due to an active Mediterranean storm track, reduced boreal winter insolation could have favoured winter precipitation over the Mediterranean Sea region (Kutzbach et al., 2014; Magny et al., 2013; Meijer and Tuenter, 2007; Rohling, 1994). The influence of a third freshwater source, Black Sea outflow, has been estimated to be minor, since the time of Black and Mediterranean Sea connection (9 to 8 cal ka B.P., Soulet et al., 2011; Vidal et al., 2010) had occurred later than the onset of S1 deposition. Deglacial conditions were not compulsory for sapropel deposition (Rohling, 1994) even if sea-level rise and consequent incursion of deglacial fresh Atlantic water towards the eastern Mediterranean Sea have possibly contributed to surface water density decrease from 14.5 ka (Rohling et al., 2015).

In addition to orbitally driven insolation changes in a precession cycle, Mediterranean Sea bottom water oxygenation records indicate centennial to millennial variability (Abu-Zied et al., 2008; Casford et al., 2003; De Rijk et al., 1999; Hennekam et al., 2014; Kuhnt et al., 2007; Rohling et al., 1997; Schmiedl et al., 2010). One of the most prominent changes occurred around 8 cal ka B.P., mainly affecting shallow water masses (Rohling et al., 2015) at water depths ≤ 1500 m in the South Aegean Sea (ex. sites SL123 and LC-21, Figure 1a and b) and ≤ 1200 m in the Adriatic Sea (ex. MD90-917, not shown in figure; Siani et al., 2013). Both internal processes such as winter cooling in the northern high latitudes (Schmiedl et al., 2010) and solar activity (Hennekam et al., 2014; Rohling et al., 2002) have been proposed to produce centennial to millennial variability in the eastern Mediterranean Sea.

The spatiotemporal distribution of S1 deposition in the eastern Mediterranean Sea could provide further insight into the water column structure during Holocene. A compilation study revealed a presence of anoxic boundary at about 1,800 m in water depth (De Lange et al., 2008). However, the stability of this boundary from early to mid-Holocene is poorly

known. Regional-scale modelling studies allowed an examination of the physical and biogeochemical processes behind S1 formation (Adloff, 2011; Adloff et al., 2011; Bianchi et al., 2006; Grimm, 2012; Meijer and Tuenter, 2007) but proxy reconstructions that can be compared with simulations are still scarce for the Holocene. This is because, under low oxygen conditions, conventional approaches such as benthic foraminiferal $\delta^{13}C$ measurements suffer from epibenthic foraminifera paucity (Jorissen, 1999). Bulk sediment geochemistry provides complementary information when post-depositional elemental redistribution is carefully considered (Calvert and Fontugne, 2001; Reitz et al., 2006; Thomson et al., 1995; Thomson et al., 1999; van Santvoort et al., 1996).

In this study, we investigated bottom water oxygenation conditions using a core MD04-2722 (33°06'N, 33°30'E, 1,780 m water depth, Figure 1) by analyzing major, minor and trace elemental concentrations within bulk sediments obtained from XRF (X-Ray Fluorescence) scanning and ICP-MS measurements. Stable isotopic analyses of the surface dwelling planktonic foraminifer *Globigerinoides ruber* (white) and benthic foraminiferal abundance were also conducted. Based on twelve ^{14}C dates of *G. ruber*, we established well-dated high-resolution records to provide a bottom water ventilation history for the deep eastern Mediterranean Sea associated with S1 deposition.

2. Modern Mediterranean circulation and the study area

Present-day Mediterranean Sea thermohaline circulation is characterized by an anti-estuary pattern (Tomczak and Godfrey, 1994). Atlantic surface water enters the surface western and eastern Mediterranean Sea by passing through the Gibraltar and Siculo-Tunisian Straits, respectively. Through excess evaporation, the salinity of surface water continues to increase, forming Modified Atlantic Water (MAW). In the Levantine Sea (Figure 1a), MAW flows along the African coast off the Nile River then around Cyprus (Pinardi and Masetti,

2000). Between Cyprus and Rhodes, MAW is cooled by cold winter winds and can be transformed into Levantine Intermediate Water (LIW, 14ºC, salinity of 38.7, with a potential density anomaly σ_o = 29.05 kg/m^3, Figure 1b) (Tomczak and Godfrey, 1994). The water mass occupies 200-500 m in the Levantine Sea and consists of the major water mass flowing back toward the western Mediterranean Sea through the Siculo-Tunisian Strait (Tomczak and Godfrey, 1994). Deep water found in the eastern Mediterranean Sea is an admixture consisting of LIW and Adriatic Sea surface water cooled by winter Bora winds (Tomczak and Godfrey, 1994). This Eastern Mediterranean Deep Water (EMDW, 13ºC, salinity of 38.6, σ_o = 29.19 kg/m^3, Figure 1b) is less saline but colder and denser than LIW, bathing below 600 m in the eastern basin (Tomczak and Godfrey, 1994). In addition to the Adriatic Sea, deepwater formation was observed in the Aegean Sea in the 90s due to increased salinity (Roether et al., 1996). Activity in the zone as the site of deepwater formation is poorly known for the Holocene.

At the location of core MD04-2722, surface water corresponds to the MAW and the bottom water mass is estimated to be EMDW (Figure 1b).

3. Materials and methods

3.1. Materials

Core MD04-2722 (33°06'N, 33°30'E, 1,780 m water depth, total core length of 36.96 m) was collected in the south of Cyprus in the eastern Levantine Sea (Figure 1a) during the VANIL cruise (R/V Marion Dufresne) conducted in 2004. In this study, we investigated the first 2.5 m of sediments that covers the past 23.6 cal ka B.P. (Section 4). The sediment is composed of a mixture of biogenic and fine terrigenous fractions (E. Ducassou, personal communication, 2014). The first 48 cm of the sediments is homogeneous and presents bioturbated hemipelagic mud facies. In the 48 to 62 cm interval, the core is brown with

typical oxidized sediments. The boundary surrounding 62 cm is not completely horizontal due to sediment heterogeneity and/or coring processes. From 62 to 118 cm, sediments are dark green with an oily aspect and do not contain visible laminations. The interval from 118 to 250 cm consists of bioturbated hemipelagic mud facies. The colour of sediments is represented in grayscale values (Figure 2).

The core was sampled at every 2 cm interval for *G. ruber* (white) for stable isotope analysis. Benthic foraminiferal abundance was studied at a 2 cm interval for the first 134 cm and with 2 to 10 cm resolution for the deeper part. XRF scanning was performed every 5 mm over the depths studied. The bulk sediment elemental composition was determined at a 2 cm interval for 40 to 160 cm, and at a 4 to 20 cm interval for other depth ranges.

3.2. Analytical methods

All analyses were performed at CEREGE. High-resolution, non-destructive elemental analyses were performed using an XRF core scanner (ITRAX, Cox Analytical Systems). The relative abundance of S, Cl, Fe, Ti, V, Ca, Mn, and Br was measured under different conditions. For Mn, V and Br measurements, a Mo tube was used as the X-ray source at 30 kV and 40 mA with 20 seconds of counting. For other elements, a Cr tube was used at 30 kV and 30 mA with 20 seconds of counting. From the high-resolution optical image obtained by ITRAX, a grayscale profile was extracted using ImageJ software (http://imagej.nih.gov/ij/).

To determine the concentrations of Al, Ca, Ti, Fe, Mn, Ba, Mo, U, V, As, Sb, Ni, Co, Cu and Li in bulk sediments, well-homogenized, freeze-dried sediments (30 mg) were totally dissolved in a mixture of ultrapure acids (1.7 ml of 15 M HNO_3, 1.3 ml of 22M HF and 0.1 ml of $HClO_4$). Obtained solutions were diluted and analyzed by an ICP-MS (Agilent 7500ce). The accuracy of measurements was estimated using analyses of geostandards MAG-1 (marine mud) and GSD12 (river sediment) that were subjected to the same digestion protocol as

151 samples. The analytical uncertainty was less than 5% and blank levels for the digestion
152 procedure were lower than 2% of the mean measured concentration for all of the analyzed
153 elements.

154 Calcite tests of *G. ruber* (white) were picked from the 250-355 μm size-fraction.
155 Foraminiferal $\delta^{18}O$ and $\delta^{13}C$ measurements were performed on a mass spectrometer (Finnigan
156 Delta Advantage) equipped with a carbonate device. The measured isotopic values were
157 normalized against NBS19. Mean external reproducibility was better than 0.05‰.

158 Benthic foraminifera abundance was determined by counting all existing calcareous
159 specimens in the >150 μm size fraction and dividing the number by the corresponding dry
160 bulk sediment weight. Since the benthic foraminiferal abundance became very high in
161 sediments below 134 cm, total benthic foraminiferal numbers were only counted for the first
162 132 cm. Dominant benthic foraminiferal species were identified for the studied interval.

163

164 **4. Chronology**

165 Chronology of core MD04-2722 is based on twelve AMS ^{14}C ages performed at the
166 ARTEMIS facility (Gif-sur-Yvette, France) on *G. ruber* (white) obtained from the >150 μm
167 size fraction. Conventional radiocarbon ages were converted into calendar ages based on
168 MARINE13 (Reimer et al., 2013) using the ^{14}C calibration software CALIB 7.0.1 (Stuiver
169 and Reimer, 1986-2013) (Table 1). The calibration integrates a marine ^{14}C reservoir age of
170 400 years that agrees well with Mediterranean Sea surface water radiocarbon reservoir age of
171 390 ± 85 years (Siani et al., 2000; Siani et al., 2001).

172 The estimated mean sedimentation rate was 12 cm/ka. According to the age model, the
173 typical temporal resolution for XRF measurements (5 mm), stable isotopes (2 cm), and ICP-
174 MS measurements (2 to 10 cm) is approximately 40 years, 170 years, and 170 to 800 years,
175 respectively.

5. Results

For the studied interval, the Al and Ca concentrations in bulk sediments ranged between 4.4 and 6.9% and between 10 and 17%, respectively (not shown in the figure). Based on the assumption that the Al concentration in the detrital fraction was 8.0% (upper continental crust; McLennan, 2001) and that all Ca was in the form of $CaCO_3$, we roughly estimated that the two major components in the bulk sediments were detrital (55 to 86%) and carbonate (25 to 42%) fractions. Considering the high proportion for the detrital component, enrichment of the analyzed elements was evaluated using normalization against Al. By taking into account the difficulty of precisely analyzing Al due to the attenuation of the XRF signal by pore water (Tjallingii et al., 2007), a Ti normalization was used for the XRF results .

5.1. Evaluation of the S1 layer

In core MD04-2722, the preserved S1 layer was visually recognized as the dark color between 60 and 120 cm with the slightly lighter colour interval from 80 to 100 cm shown in the grayscale profile (Figure 2). High-resolution variability in organic matter content was shown by a Br/Cl ratio profile obtained from a XRF scan (Figure 2). Although Br XRF intensity and Br/Cl ratio presented very similar variability (not shown in figure), we used the Br/Cl XRF intensity ratio to better illustrate changes in the organic matter content (Cartapanis et al., 2014) since Br is incorporated in marine organic matter but also exists in pore water (Cartapanis et al., 2011; Ziegler et al., 2008). High Br/Cl ratio values were found in the 55 to 120 cm interval and a clear decrease existed between 60 and 110 cm (Figure 2). Below 120 cm, the Br/Cl ratio was low and comparable to the core-top value (Figure 2).

Barium enrichment has often been used to localize initial sapropel layers, since it is associated with biogenic barite ($BaSO_4$) that is an export production proxy resistant to post-

depositional oxidation (Calvert and Fontugne, 2001; De Lange et al., 2008; Thomson et al., 1995; Thomson et al., 1999; van Santvoort et al., 1996). Both the Ba concentration and Ba/Al ratio in core MD04-2722 displayed a similar convex-shaped peak from 55 to 120 cm, consistent with the high Br/Cl ratio interval (Figure 2). The depth range of high Ba and organic matter content at 55 to 120 cm corresponded to 6.8 to 10.4 cal ka B.P. (Table 1). This time span is, in general, in agreement with the previously estimated S1 deposition period of 6.1 ± 0.5 to 10.8 ± 0.4 cal ka B.P. (De Lange et al., 2008).

Close to the upper end of the Ba/Al ratio peak, prominent Mn enrichment was found at 56 to 60 cm (6.8 to 7.0 cal ka B.P.) for both the Mn/Al and Mn/Ti ratio profiles (Figure 2). The peak shape of Mn/Al and Mn/Ti ratios was slightly different around 62 cm, possibly due to different sampling resolutions (1 cm for the Mn/Al ratio and 5 mm for Mn/Ti ratio) and the irregular brown-coloured boundary at approximately 62 cm (see section 3.1). As the Mn peak is mainly associated with the precipitation of Mn oxides under improved oxygenation, it often marks the end of S1 (Reitz et al., 2006). Taken together, we defined the S1 layer of core MD04-2722 at 55 to 120 cm (the dark gray band in Figure 2).

The number of benthic foraminifera gradually increased from the core-top to 56 cm and reached a maximum value at 56 to 58 cm, with the Mn peak (Figure 2). Between 55 and 142 cm, benthic foraminiferal abundance displayed a concave shape (Figure 2). In the S1 layer, the sediment was void of benthic foraminifera at 104 cm (9.2 cal ka B.P.) and 108 cm (9.4 cal ka B.P.). Below 142 cm (12.6 cal ka B.P.), benthic foraminiferal abundance was higher than for the upper part. Major species identified within the studied interval included *Gyroidina spp., Cibicidoides pachyderma, Hoeglundina elegans*, *Cibicidoides wuellestorfi, Uvigerina spp*., *Bolivina spatulata,* and *Globobulimina spp*. (not shown in the figure). The first appearance of *Globobulimina spp*., indicators of low oxygen content (Jorissen et al.,

225 1995) is at 138 cm (12.2 cal ka B.P.). A detailed faunal assemblage will be provided
226 elsewhere.
227
228 **5.2. Indicators of dry/wet conditions**
229 The major detrital fraction in the study area originated from the Nile River particles
230 and Saharan dust (Krom et al., 1999). Ti/Al values have been used as an indicator of the
231 relative proportion of Nile River particles to Saharan dust (Wehausen and Brumsack, 2000;
232 Ziegler et al., 2010). In general, due to greater inputs of Al-rich river particles as compared to
233 the contribution of Ti-rich dust inputs (Wehausen and Brumsack, 2000; Ziegler et al., 2010),
234 the Ti/Al ratios of sediments far from the coastal zones in the eastern Mediterranean Sea were
235 lower under wet conditions. Ti/Al values in core MD04-2722 varied from 0.07 to 0.09 g/g for
236 the upper 250 cm with lower values between 35 and 230 cm (5.4 to 22.1 cal ka B.P.) (Figure
237 2).
238 In addition to Ti/Al ratios, *G. ruber* $\delta^{18}O$ values reflect wet/dry conditions and also
239 cool/warm surface water temperatures and continental ice volume. The isotopic values of core
240 MD04-2722 ranged between -1.4‰ and 3.5‰ with minimum and maximum values at 112 cm
241 (9.6 cal ka B.P.) and 220 cm (21.3 cal ka B.P.), respectively (Figure 2). The interval for low
242 *G. ruber* $\delta^{18}O$ values roughly agreed with the low Ti/Al interval (Figure 2).
243
244 **5.2. Redox sensitive elements**
245 Due to pyrite formation under reducing conditions, the sulphur content of bulk
246 sediments is high in sapropel layers (Passier et al., 1996; Rohling, 1994). Considering that
247 sulphur also exists in pore water in the form of the sulphate ion, we used the S/Cl ratio in core
248 MD04-2722 to extract a signal closely related to pyrite even if S XRF intensity and S/Cl
249 presented virtually identical profiles (not shown in figure). S/Cl values in core MD04-2722

250 indicated variability similar to the Ba/Al ratio (Figure 3) but enrichment below the S1 layer at
251 120 to 150 cm (the darkest gray band in Figure 3). This enrichment can be explained by
252 downward sulphidisation (see section 6.1). The downward sulphidisation could account for
253 high values for the S/Cl, Ni/Al, As/Al and Fe/Al ratios below the S1 layer (Figure 3) since As
254 and Ni (and also Co and Cu) are often adsorbed and/or incorporated in pyrite (Large et al.,
255 2014).

256 In general, high sedimentary Ni, Co and Cu concentrations are produced by enhanced
257 productivity via the transfer of these elements due to the organic matter flux and fixation in
258 sediments under reducing environments (Cartapanis et al., 2011; Nameroff et al., 2002). Ni/Al
259 values in core MD04-2722 were higher inside and below the S1 layer (Figure 3). The Co/Al
260 and Cu/Al ratios indicated variability comparable to the Ni/Al ratio (not shown in the figure).

261 A remarkable feature of the As/Al and Fe/Al profiles was strong depletion centred at
262 82 to 84 cm (around 8 cal ka B.P. inside the light gray band in Figure 3). Depletion was also
263 observed for the V/Al profile with a wider depth range between 80 and 110 cm (7.9 to 9.5 cal
264 ka B.P.) (Figure 3).

265 The U, Mo and Sb content of core MD04-2722 indicated a clear peak centred at the
266 interval of the high Ba/Al ratio but a detailed structure was specific to each element (Figure
267 3). The U/Al profile indicated a smooth convex shape between 60 and 148 cm (7.0 to 13.2 cal
268 ka B.P.), with a small negative spike at 84 cm (8.2 cal ka B.P., inside the light gray band in
269 Figure 3). The main peak for the Mo/Al and Sb/Al ratios ranged between 70 and 138 cm (7.6
270 to 12.2 cal ka B.P.), and 50 and 138 cm (6.3 to 12.2 cal ka B.P.), respectively (Figure 3). The
271 Mo/Al and Sb/Al ratios indicated a sharp peak from 56 to 60 cm where the benthic
272 foraminiferal number (Figure 2) and the Mn content were at a maximum (the orange band in
273 Figure 3). In addition to the Mo/Al and Sb/Al ratios, the Li/Al ratios of core MD04-2722
274 presented a peak synchronous with the high Mn content (Figure 3).

6. Discussion

Redox-sensitive elements and benthic foraminiferal abundance in core MD04-2722 can be used as an indicator of bottom/pore water conditions which, in turn, are modulated by bottom water ventilation and biological productivity, whereas the Ti/Al ratio and *G. ruber* $\delta^{18}O$ records reflect wet/dry conditions. In the following discussion, we first describe the geochemical meaning of the different elemental ratios that can be used to infer Mediterranean Sea ventilation. We then propose deepwater conditions for the onset, during and at the termination of S1 deposition by combining the whole obtained data.

6.1. Geochemical meaning of elemental ratios

During sapropel deposition, sulphate reduction occurred, and HS^- excess for pyrite precipitation migrated downwards whereas pore water Fe^{2+} existing below sapropel layer moved upwards, leading to pyrite precipitation (Passier et al., 1996). The process is called downward sulphidisation and impacts the distribution of trace elements such as Ni, Co, As and Cu associated with pyrite (Passier et al., 1996). Hence, the enrichment of Ni, Co and Cu below the S1 interval may not signify an increase in biological productivity prior to S1 deposition. Considering the difficulty in interpreting peaks below the S1 layer, here, we do not discuss them further.

Due to insoluble chemical speciation in reducing environments, authigenic U and Mo accumulate under suboxic and anoxic conditions, respectively (Algeo and Maynard, 2004; Klinkhammer and Palmer, 1991; Tribovillard et al., 2006). The accumulation of these elements does not necessarily indicate that the bottom water was permanently highly depleted in oxygen. Enrichment could reflect suboxic/anoxic pore water conditions related to slow ventilation and/or high organic rain. Taking this fact into account, we carefully evaluated

potential circulation changes by combining the U/Al and Mo/Al profiles of core MD04-2722 (Figure 3) with results from previous studies (see section 6.2).

In the middle of the S1 unit, the sediment colour was lighter and the sedimentary organic matter (Br/Cl ratio) and redox sensitive element (Fe/Al, As/Al and V/Al ratios) were lower (light gray band in Figures 2 and 3). The observed change could be explained by the injection of dissolved oxygen into the water column via re-ventilation. The oxidation of organic matter within the water column and on the sea floor can reduce sedimentary Br/Cl values. The pyrite in sediments can be oxidized to iron oxides and/or to hydroxides when it is in contact with dissolved oxygen (Chandra and Gerson, 2011). If these oxides and/or hydroxides are again reduced in sediments, Fe and As associated with pyrite would be released to pore water. Vanadium accumulation in anoxic sediments commonly takes place via diffusion across the sediment/water interface and the release of this element occurs when Mn is reduced (Nameroff et al., 2002). We investigate this issue in section 6.3.

The origin of the Mn peak at the end of S1 has been extensively discussed in previous studies (Reitz et al., 2006; Thomson et al., 1995; Thomson et al., 1999; van Santvoort et al., 1996). Core MD04-2722 only contains one Mn peak at the end of the S1 unit (Figure 2) and the Mo/Al, Sb/Al and Li/Al ratios synchronously increase with Mn (Figure 3). Since Mo (Shimmield and Price, 1986; Tribovillard et al., 2006), As (Cutter et al., 2001 and references therein) and Li (Reitz et al., 2006) can be scavenged by Mn oxides, the peaks observed for core MD04-2722 were likely produced from water column oxygenation at the S1 termination (section 6.4).

The following discussion focuses on the state of bottom water circulation in the deep eastern Mediterranean Sea during the following periods: (i) the onset of S1 deposition, (ii) oxygenation event(s) in the middle of the S1 unit, and (iii) the termination of S1 deposition. We are aware that, due to diagenetic processes and post-despositional diffusion that can

modify boundary positions, precise timing for ventilation changes is difficult to obtain from a single proxy profile. Considering the fact that distribution of each element is determined by element-specific processes, we interpret and discuss the timing of ventilation changes when several proxy reconstructions indicate consistent changes.

6.2. Conditions of bottom water circulation prior to S1 deposition

In core MD04-2722, U/Al and Mo/Al ratios began to increase from 13 cal ka B.P. (148 cm) to 12 cal ka B.P. (138 cm, Figures 3 and 4). This time span corresponds also to the beginning of decrease in benthic foraminiferal number (12.2 cal ka B.P., 138 cm; Figures 2 and 4) that was high in well-oxygenated glacial bottom waters. Two major factors affecting benthic foraminiferal assemblage are food supply and water oxygenation (Jorissen et al., 1995). Since the Ba/Al change indicates increasing trend of export production just before the S1 deposition (Figure 2), it is logical to assume that the observed reduction of benthic foraminiferal number was related to oxygen depletion. Therefore, the result can be interpreted as the onset of oxygen depletion for bottom and/or pore waters at 1,780 m in water depth started prior to S1 deposition. Since surface water freshening has been considered to be the main factor affecting Mediterranean Sea thermohaline circulation (De Lange et al., 2008; Emeis et al., 2000; Rohling, 1994), we examine timing for the onset of wet conditions, changes in surface hydrology, and deepwater circulation using records obtained from core MD04-2722.

Decreases for the Ti/Al ratio and *G. ruber* $\delta^{18}O$ in core MD04-2722 began prior to S1 deposition (Figure 4). To better illustrate surface water salinity changes in the Levantine Sea, the *G. ruber* $\delta^{18}O$ record is combined with sea surface temperature (SST) reconstruction that is based on planktonic foraminiferal assemblages obtained from a vicinity site (core MD84-632, 32º28'N, 34º13'E; Essallami et al., 2007; Figure 1a). The present-day bottom water $\delta^{18}O$

350 value (Pierre, 1999) is then subtracted so that the local $\delta^{18}O_w$ anomaly can be calculated
351 (Figure 4). A marked decrease in the $\delta^{18}O_w$ anomaly began at approximately 12 cal ka B.P.
352 (Figure 4). Variability mainly stems from the core MD04-2722 *G. ruber* $\delta^{18}O$ record, not on
353 temperature because the major feature is maintained when another SST record from a nearby
354 site is applied (Castañeda et al., 2010). We note here that the large amplitude of seawater $\delta^{18}O$
355 anomaly change of 2.7‰ from 20.1 to 9.6 cal ka B.P. cannot be explained by global $\delta^{18}O$
356 change related to continental ice volume (Waelbroeck et al., 2002). Another record of *G.*
357 *ruber* $\delta^{18}O$ from a close site (core MD84-641; 33°02′N; 32°28′E, 1,375m water depth)
358 (Fontugne and Calvert, 1992) indicates a very similar variability to the core MD04-2722
359 record, attesting that the *G. ruber* $\delta^{18}O$ variability represents regional hydrological changes.
360 The $\delta^{18}O_w$ anomaly and Ti/Al records indicate the beginning of a fresher and wetter
361 period at approximately 12 and 15 cal ka B.P., respectively, comparable with the inception of
362 the African humid period at 12.5 cal ka B.P. (Adkins et al., 2006; deMenocal et al., 2000) and
363 increased Nile River discharge (Revel et al., 2014) in response to insolation changes (Laskar
364 et al., 2004) (Figure 4). Our result is consistent with the hypothesis that Nile River discharge
365 was one of the main fresh water sources for the Levantine Sea (Rossignol-Strick et al., 1982).
366 Indeed, the influence of Nile River discharge was estimated to have spread as far as Cyprus
367 (Almogi-Labin et al., 2009) (Figure 1a).
368 Spatial extension of weakly ventilated waters can be evaluated by comparing with
369 previously reported records from the eastern Mediterranean Sea. Based on the U-Th dating of
370 authigenic carbonates formed in reducing environments, the start of suboxic bottom water
371 conditions was estimated to be 12 cal ka B.P. on the Nile River deep-fan at 1,160 m in water
372 depth ("buildups"; Bayon et al., 2013) (Figures 1ab and 4). Based on decreasing benthic
373 foraminiferal $\delta^{13}C$ values that began at 15 cal ka B.P (Figure 4), weaker ventilation has also
374 been estimated for a water depth of approximately 700 m in the south Aegean Sea (site

375 SL123) and for a water depth of approximately 900 m in the southeast Levantine Sea (site
376 SL112) (Kuhnt et al., 2007; Schmiedl et al., 2010) (Figure 1ab). It is worth noting that the
377 decreasing trend of foraminiferal benthic $\delta^{13}C$ values does not necessarily mean complete
378 shutdown of ventilation. The $\delta^{13}C$ values (Figure 4) were still comparable with the late
379 Holocene values, and both benthic foraminiferal assemblage and trace elements (Figure 5) did
380 not indicate strong anoxic conditions before S1 interval. We thus propose reduced
381 intermediate/deepwater formation and consequently restricted extension of well-oxygenated
382 water mass(es) for this period. Productivity change is estimated to have a second role because
383 it would be more local/regional, reflecting coastlines, local nutrient supplies such as riverine
384 inputs, and the topography of lands that impact wind regimes.

385 The net increase in fresh water inputs reinforced vertical salinity gradients in the
386 Eastern Mediterranean Sea, which in turn shoaled the pycnocline at a depth shallower than the
387 euphotic layer, allowing the development of a deep chlorophyll maximum relative to present
388 day in the easternmost Mediterranean Sea (Castradori, 1993; Grelaud et al., 2012; Rohling,
389 1994). A shoaling pycnocline and a greater nutrient supply due to Nile River discharge (Herut
390 et al., 2000) could have contributed to enhanced biological productivity. Considering the time
391 required for circulation reorganization, the gradual consumption of existing dissolved oxygen
392 in the water column by organic decomposition, and the improvement of sedimentary organic
393 matter preservation under oxygen-depleted conditions (Hartnett et al., 1998), it is not
394 surprising that a net increase in the Br/Cl ratio in core MD04-2722 appeared later than the
395 onset of slow bottom water circulation (Figures 2 and 3).

396 Recent regional-scale modelling studies have proposed that initial glacial conditions
397 were a key parameter for forming S1 deposition (Adloff, 2011; Grimm, 2012). Sensitivity
398 experiments indicate that fresh water contributions and increased productivity are not
399 sufficient for attaining the observed bottom water oxygen depletion (Adloff, 2011; Grimm,

2012). Only a simulation that considered initial glacial conditions succeeded in maintaining oxygen-depletion for several thousand years that were comparable to S1 duration (Grimm, 2012). The inception of weaker ventilation during the glacial-interglacial transition, as proposed in this study, is in line with these recent simulations.

6.3. Re-ventilation in the middle of the S1 period

The lighter colour of the sediment and the clear decrease in the Br/Cl (Figure 2), As/Al, Fe/Al and V/Al ratios (Figure 3) in core MD04-2722 indicate temporally improved oxygenation in the water column and in pore water in the middle of the S1 period. Since the Ba/Al ratio did not show clear diminution at this interval (Figure 2), biological productivity was not responsible for the change. Improved oxygenation seems to be related to an active re-ventilation that promoted organic matter degradation in the water column and post-depositional oxidation (Thomson et al., 1999). To examine the variability in detail, we combine highly resolved Br/Cl, Fe/Ti and V/Ti records with Fe/Al, As/Al and V/Al ratios (Figure 5). The major decline in the Fe/Al, Fe/Ti and As/Al ratios is centred at 8.4 to 8.2 cal ka B.P., whereas minimal Br/Cl, V/Al and V/Ti ratios extended between 9.5 to 7.9 ca ka B.P. (Figure 5). A longer depletion period for the Br/Cl, V/Al and V/Ti ratios can be explained by continuous organic matter oxidation with oxygen penetrated into sediments as well as the subsequent reduction of Mn oxides (see section 6.1).

Our results indicate that re-ventilation event(s) affected bottom water located at the upper limit of the anoxic layer at 1,800 m (De Lange et al., 2008). By combining the results of core MD04-2722 with previously reported high-resolution records, we examine the spatial coverage of re-oxygenation. In addition to shallow Adriatic Sea (MD90-917, 41°17'N, 17°37' E, 1,010 m, not shown in the figure; Siani et al., 2013) and shallow south Aegean Sea (sites LC-21 and SL123 ≤ 1500 m; Fig. 1), benthic foraminiferal assemblage indicates re-ventilation

425 in the Levantine Sea at water depths ranging from 900 m (site SL112, Fig. 1; Schmiedl et al.,
426 2010) to 2,300 m (site LC-31, Fig. 1; Abu-Zied et al., 2008; Schmiedl et al., 2010). We
427 propose two hypotheses about re-ventilation depths. Firstly, the re-ventilation affected water
428 column down to 2,300 m. The second possibility is the re-ventilation was limited to water
429 depths shallower than 1,800 m taking into account the fact that core LC-31 contains a small
430 slump confirmed by AMS ^{14}C dates inside of the S1 layer (Abu-Zied et al., 2008). In any
431 case, the large spatial distribution of the S1 interruption at least as deep as 1,780 m suggests a
432 basin-wide reorganization for ventilation.

433 Cores presenting the S1 interruption are currently bathed in well-oxygenated EMDW
434 (Figures 1b and 5). At present, the formation of EMDW is controlled by the winter cooling of
435 surface water in the Adriatic Sea and occasionally in the Aegean Sea (Roether et al., 1996), as
436 well as by the salinity of LIW (section 2). Holocene surface water winter cooling in the
437 Aegean Sea has been demonstrated to occur with atmospheric circulation changes in relation
438 to the winter and spring Siberian High at 9.5 to 9.1 and 8.8 to 7.8 ka (Kotthoff et al., 2008;
439 Marino et al., 2009; Mayewski et al., 1997), and for the 8.2 ka event (Pross et al., 2009)
440 recorded in Greenland ice cores (Alley and Ágústsdóttir, 2005). Due to the cold air flux from
441 polar regions, surface water in convection zones could be cooled during winter, leading to the
442 activation of deep water formation in the Aegean (Schmiedl et al., 2010) and/or the Adriatic
443 (Siani et al., 2013) Seas. A numerical simulation has indicated that a surface eastern
444 Mediterranean Sea cooling of 2-3 ºC could trigger deep convection in the Adriatic Sea and
445 intermediate water formation in the Aegean Seas, leading to oxygenation for the upper 1,250
446 m water masses of the eastern Mediterranean Sea (Myers and Rohling, 2000)

447 On the other hand, reconstructed Nile River discharge (Figure 4) presented a high-
448 frequency variability and a decline around 8 cal ka B.P. (Blanchet et al., 2014; Revel et al.,
449 2014) . Planktonic foraminiferal Ba/Ca ratios indicate the fluctuation in Nile River discharge

450 at 8.4-8.2 cal kyr B.P. (Weldeab et al., 2014). Reduced Nile River discharge could have led to
451 a salinity rise for LIW that mixed with surface Adriatic Sea water, contributing to the
452 activation of EMDW formation. Thus, both temperature and salinity effects could be factors
453 for re-ventilation in the eastern Mediterranean Sea (Figure 6) in relation to northern high
454 latitude and tropical/subtropical climate conditions.

455 During the interruption period, vertical density gradient was attenuated, leading to
456 partial mixing between old dense glacial waters and overlaying lighter waters. Once cooling
457 and/or reduced fresh water input finished, the stagnant ventilation mode came back, which
458 suggests that the density barrier was still too strong to shift to the present-day circulation
459 mode. If the duration of cooling/less fresh water inputs, the size of this forcing and the
460 spatiotemporal S1 interruption are quantified, interruption can provide information regarding
461 the sensitivity of eastern Mediterranean thermohaline circulation.

462

463 **6.4. Total ventilation recovery at the S1 termination**

464 Mn/Al, Mn/Ti, Mo/Al, Li/Al and Sb/Al ratios (Figure 3), as well as the benthic
465 foraminiferal abundance of core MD04-2722 (Figure 2), indicated a synchronous increase at
466 7.0 cal ka B.P. (60 cm) to 6.8 cal ka B.P. (56 cm), suggesting oxygenation in the water
467 column at the core location. The age range for the increase was slightly earlier than the basin-
468 wide S1 termination of 6.1 ± 0.5 cal ka B.P. that was estimated using the cores from water
469 depths down to 3400 m (De Lange et al., 2008) although, considering the dating uncertainty,
470 the difference was subtle. If the age difference is real, the S1 termination may be
471 characterized by depth-dependant ventilation recovery with earlier oxygenation at depths
472 shallower than 1,800 m. Based on previous observations, we suggest this possibility. At first,
473 benthic ecosystem recovery at the S1 termination was depth-dependent, with a prior recovery
474 at shallower depths in the eastern Mediterranean Sea (Schmiedl et al., 2010). The second

475 point is the possible existence of dense deep water. Modelling studies have indicated that the
476 deep water mass was much denser than that of shallower waters because they contained saline
477 glacial (Grimm, 2012; Myers et al., 1998) (Figure 6). If the increase in surface water density
478 did not exceed the density of this dense water below, ventilation would affect only lighter
479 water masses at shallower depths.

480 Ventilation recovery can be explained both by the reduction of riverine fresh water
481 inputs and surface water cooling. A 9,000-yr-long transient model with insolation and
482 atmospheric greenhouse gas forcing simulated a gradual precipitation decline over eastern
483 Africa from the early to late Holocene (Renssen et al., 2006). Reconstructed Nile River
484 discharge (Blanchet et al., 2014; Revel et al., 2014; Weldeab et al., 2014) displayed a
485 decreasing trend from the early to mid-Holocene (Figure 4). Approximately 3ºC of the SST
486 decrease during April-May was recorded in the south Adriatic between 7.1 and 6.9 cal ka BP
487 (Siani et al., 2013). In the south Aegean Sea during winter, an approximate 2 to 3 ºC in
488 surface water cooling was observed from 7.5 to 7.0 cal ka B.P. (Marino et al., 2009). Once
489 surface water density within the deep/intermediate water formation zones exceeded the
490 threshold value, water convection could restart. The onset of these cooling records is
491 consistent with our estimation for total ventilation recovery at water depths shallower than
492 1,800 m from 7.0 to 6.8 cal ka B.P.

493 Considering the subtle density difference between the present LIW and EMDW
494 (section 2) and distinct climate background between the present and the moment of S1
495 termination, it is unattainable to precisely identify physical mechanisms of total ventilation
496 recovery. Nonetheless, if ventilation recovery was water depth dependent, the S1 termination
497 contrasted with re-ventilation event(s) during the S1 period, affecting waters below the
498 critical depth of 1,800 m in the Levantine Sea (Figures 5 and 6). The finding provides new
499 constraints for vertical structure within the eastern Mediterranean Sea during S1 deposition.

500

501 **Conclusions**

502 We analyzed the bulk sediment elemental composition, the $\delta^{18}O$ of *Globigerinoides*
503 *ruber* and the abundance of benthic foraminifera since the last deglaciation within core
504 MD04-2722 obtained from the Levantine Sea. Water depth at the core location was close to
505 the estimated anoxic layer upper limit for the most recent sapropel S1 depostion, 1,800 m, and
506 rendered the site highly sensitive to past circulation changes. By combining our new results
507 with previous studies, some fundamental features for ventilation in the eastern Mediterranean
508 Sea were identified.

509 Bulk sediment Ti/Al ratios and the surface water $\delta^{18}O$ anomaly calculated from the *G.*
510 *ruber* $\delta^{18}O$ obtained from core MD04-2722 indicated that a wet period and fresher surface
511 water appeared at the core site around 15 to 12 cal ka B.P. The enrichment of Mo and U, as
512 well as benthic foraminiferal density indicated that surface hydrological changes were
513 transferred to bottom water, leading to the reduction of intermediate/deep water formation and
514 consequent restricted expansion of oxygenated that began prior to S1 deposition. Our results
515 are consistent with previous reconstructions and regional-scale simulations, and support the
516 idea that reduced oxygen supply due to slow ventilation was a precondition of S1 formation.

517 Decreased Br/Cl, Fe/Al, Fe/Ti, V/Al, V/Ti and As/Al ratios indicated that temporal re-
518 oxygenation event(s) occurred during the middle of the S1 period. Improved oxygenation was
519 produced by active re-ventilation rather than reduced biological productivity and affected
520 water depths at least as deep as 1,800 m in the Levantine Basin. Winter cooling in the Aegean
521 and Adriatic Seas in relation to northern high latitude conditions and salinity increases related
522 to reduced Nile River discharge contributed to the temporal reactivation of thermohaline
523 circulation in the eastern Mediterranean Sea.

From the concomitant peak of Mn, Mo, Sb, and Li, and the increased abundance of benthic foraminifera, a total recovery in ventilation at the core MD04-2722 site was estimated to have occurred at 7.0 to 6.8 cal ka B.P. We tentatively propose a depth-dependent S1 termination with an earlier ventilation at water depths shallower than 1,800 m. This study provides new constraints for the eastern Mediterranean Sea bottom water circulation since the last deglaciation that could be examined by future modelling studies.

Acknowledgements

This research was funded by MISTRALS/PALEOMEX meta-programme, the ANR HAMOC (ANR-13-BS06-0003) projects, the European Community (Project Past4Future), Labex OT-Med (n° ANR-11-LABX-0061), and the *MIDEX project (n° ANR-11-IDEX-0001-02). Radiocarbon dating was performed at the LMC14 laboratory as a part of the French Artemis program. We thank Emanuelle Ducassou for the core description and Laetitia Licari for identifications and discussions regarding benthic foraminifera. Majid Shah-Hosseini is thanked for sample preparation. Two anonymous reviewers are acknowledged for the constructive comments.

Figure captions

Figure 1. The core location map. (a) The core MD04-2722 (33°06'N, 33°30'E, 1,780 m water depth) location on the bathymetry map. Site locations of the records discussed in the text are as follows: MD84-632 (32º28.2'N, 34º13.2'E) (Essallami et al., 2007); MD84-641 (33°02′N; 32°28′E) (Fontugne and Calvert, 1992); SL123 (35º45.3'N, 27º33.3'E, 728 m water depth); SL112 (32º44.5'N, 34º39.0'E, 892 m water depth) (Kuhnt et al., 2007); LC-21 (35º39.7'N, 26º35.0'E, 1,520 m water depth); LC-31 (34º59.8'N, 31º09.8'E, 2,300 m water depth) (Schmiedl et al., 2010); "buildups" (32º22'N, 31º42'E, 1,160 m water depth) (Bayon et al.,

549 2013). (b) The present-day density anomaly transect along the dashed blue line at 34.5-35.5N
550 in Figure 1a. The seawater temperature and salinity are from WOA09 (Antonov et al., 2010;
551 Locarnini et al., 2010). The dashed white line indicates the upper limit of the permanent
552 anoxic layer during S1 deposition at 1,800 m (see the text for detail). Figures were generated
553 using the Ocean Data View software (Schlitzer, 2009).
554
555 Figure 2. Characterization of the S1 interval recorded in core MD04-2722. Grayscale value,
556 bulk elemental composition, benthic foraminiferal abundance (number of tests per unit of
557 weight for dry bulk sediment), *G. ruber* $\delta^{18}O$ as a function of depth in core (cm). The S1 layer
558 (55 to 120 cm) is shown with a dark gray band, the interval of low grayscale values (80 to 100
559 cm) with a light gray band, and the interval of Mn enrichment (56 to 60 cm) with an orange
560 band. Triangles indicate the depth levels dated by AMS ^{14}C (see Table 1 for details).
561
562 Figure 3. The elemental concentrations and the element/Al ratios for the bulk sediment of
563 MD04-2722 as a function of depth in core, together with the S/Cl XRF intensity. Dark and
564 light gray bands indicate the S1 layer determined from Ba enrichment (55 cm to 120 cm) and
565 the interval of low grayscale values (80 to 100 cm), respectively. The darkest gray band and
566 the orange band indicate the interval affected by downward sulphidisation (Passier et al.,
567 1996) (120 to 150 cm) and Mn enrichment (56 to 60 cm), respectively.
568
569 Figure 4. The last 23 ka variability of proxies for ventilation (U/Al, Mo/Al and benthic
570 foraminiferal density) and wet/fresh conditions (Ti/Al and seawater $\delta^{18}O$ anomaly) based on
571 core MD04-2722 results as compared with previous studies. The surface water $\delta^{18}O$ anomaly
572 was calculated by combining the *G. ruber* $\delta^{18}O$ record from core MD04-2722 with the SST
573 reconstruction (see text for detail). Suboxic conditions on the Nile deep-fan were estimated to

574 have lasted for 12 to 7 ka B.P. at the "buildups" location (Figure 1 a and 1b) (Bayon et al.,
575 2013). Benthic foraminiferal $\delta^{13}C$ records were based on the epibenthic foraminifer species
576 *Planulina ariminensis* (Kuhnt et al., 2007; Schmiedl et al., 2010). Changes in Nile River
577 discharge are shown with the log-scale Fe/Ca ratio for core MS27PT located close to the
578 Rosetta mouth of the Nile River (Revel et al., 2014). The precession parameter is from Laskar
579 et al. (2004). The blue zone indicates the African Humid Period (AHP, 12.5 to 5.5 cal ka
580 B.P.) based on Adkins et al. (2006) and deMenocal et al. (2000). The gray band indicates the
581 S1 period from 10.4 to 6.8 cal ka B.P estimated for core MD04-2722. The dashed line
582 presents the possible onset for weaker ventilation at 15 cal ka B.P. in the eastern
583 Mediterranean Sea. LGM = Last Glacial Maximum.
584
585 Figure 5. Re-oxygenation in the middle of the S1 interval as inferred from the bulk
586 geochemistry (Br/Cl, Fe/Al, Fe/Ti, As/Al, V/Al and V/Ti ratios) in core MD04-2722 and the
587 benthic foraminiferal oxygen index obtained at sites LC-31 and SL123 (Schmiedl et al., 2010)
588 (Figure 1ab). Dark and light gray bands indicate the S1 unit (10.4 to 6.8 cal ka B.P.) and the
589 interval of low grayscale values (9.0 to 7.9 cal ka B.P.) in core MD04-2722, respectively.
590
591 Figure 6. Schematic ventilation patterns in the eastern Mediterranean Sea at present, S1
592 interruption and 15-12 ka intervals.
593
594 References

595 Abu-Zied, R. H., Rohling, E. J., Jorissen, F. J., Fontanier, C., Casford, J. S. L., and Cooke, S.:
596 Benthic foraminiferal response to changes in bottom-water oxygenation and organic
597 carbon flux in the eastern Mediterranean during LGM to Recent times, Marine
598 Micropaleontology, 67, 46-68, 2008.
599 Adkins, J., deMenocal, P., and Eshel, G.: The "African humid period" and the record of
600 marine upwelling from excess 230Th in Ocean Drilling Program Hole 658C,
601 Paleoceanography, 21, PA4203, 2006.

Adloff, F.: Early Holocene Eastern Mediterranean ocean climate and the stability of its overturning circulation, PhD thesis, International Max Planck Research School on Earth System Modelling, Max Planck Institute, Hamburg, 2011.

Adloff, F., Mikolajewicz, U., Kučera, M., Grimm, R., Maier-Reimer, E., Schmiedl, G., and Emeis, K. C.: Corrigendum to "Upper ocean climate of the Eastern Mediterranean Sea during the Holocene Insolation Maximum – a model study" published in Clim. Past, 7, 1103–1122, 2011, Clim. Past, 7, 1149-1168, 2011.

Algeo, T. J. and Maynard, J. B.: Trace-element behavior and redox facies in core shales of Upper Pennsylvanian Kansas-type cyclothems, Chem. Geol., 206, 289-318, 2004.

Alley, R. B. and Ágústsdóttir, A. M.: The 8k event: cause and consequences of a major Holocene abrupt climate change, Quat. Sci. Rev., 24, 1123-1149, 2005.

Almogi-Labin, A., Bar-Matthews, M., Shriki, D., Kolosovsky, E., Paterne, M., Schilman, B., Ayalon, A., Aizenshtat, Z., and Matthews, A.: Climatic variability during the last ~90 ka of the southern and northern Levantine Basin as evident from marine records and speleothems, Quat. Sci. Rev., 28, 2882-2896, 2009.

Antonov, J. I., Seidov, D., Boyer, T. P., Locarnini, R. A., Mishonov, A. V., Garcia, H. E., Baranova, O. K., Zweng, M. M., and Johnson, D. R.: World Ocean Atlas 2009, Volume 2: Salinity. In: NOAA Atlas NESDIS 68, Levitus, S. (Ed.), U.S. Government Printing Office, Washington, D.C., 2010.

Bayon, G., Dupre, S., Ponzevera, E., Etoubleau, J., Cheron, S., Pierre, C., Mascle, J., Boetius, A., and de Lange, G. J.: Formation of carbonate chimneys in the Mediterranean Sea linked to deep-water oxygen depletion, Nature Geosci, 6, 755-760, 2013.

Bethoux, J. P. and Gentili, B.: Functioning of the Mediterranean Sea: past and present changes related to freshwater input and climate changes, J. MARINE SYST., 20, 33-47, 1999.

Bianchi, D., Zavatarelli, M., Pinardi, N., Capozzi, R., Capotondi, L., Corselli, C., and Masina, S.: Simulations of ecosystem response during the sapropel S1 deposition event, Palaeogeography, Palaeoclimatology, Palaeoecology, 235, 265-287, 2006.

Blanchet, C. L., Frank, M., and Schouten, S.: Asynchronous Changes in Vegetation, Runoff and Erosion in the Nile River Watershed during the Holocene, PLoS One, 9(12), e115958, 2014.

Calvert, S. E. and Fontugne, M. R.: On the late Pleistocene-Holocene sapropel record of climatic and oceanographic variability in the eastern Mediterranean, Paleoceanography, 16, 78-94, 2001.

Cartapanis, O., Tachikawa, K., and Bard, E.: Northeastern Pacific oxygen minimum zone variability over the past 70 kyr: Impact of biological production and oceanic ventilation, Paleoceanography, 26, PA4208, 2011.

Cartapanis, O., Tachikawa, K., Romero, O. E., and Bard, E.: Persistent millennial-scale link between Greenland climate and northern Pacific Oxygen Minimum Zone under interglacial conditions, Clim. Past, 10, 405-418, 2014.

Casford, J. S. L., Rohling, E. J., Abu-Zied, R. H., Fontanier, C., Jorissen, F. J., Leng, M. J., Schmiedl, G., and Thomson, J.: A dynamic concept for eastern Mediterranean circulation and oxygenation during sapropel formation, Palaeogeography, Palaeoclimatology, Palaeoecology, 190, 103-119, 2003.

Castañeda, I. S., Schefuß, E., Pätzold, J., Sinninghe Damsté, J. S., Weldeab, S., and Schouten, S.: Millennial-scale sea surface temperature changes in the eastern Mediterranean (Nile River Delta region) over the last 27,000 years, Paleoceanography, 25, PA1208, 2010.

Castradori, D.: Calcareous nannofossils and the origin of eastern Mediterranean sapropels, Paleoceanography, 8, 459-471, 1993.
Chandra, A. P. and Gerson, A. R.: Pyrite (FeS_2) oxidation: A sub-micron synchrotron investigation of the initial steps, Geochimica Et Cosmochimica Acta, 75, 6239-6254, 2011.
Cutter, G. A., Cutter, L. S., Featherstone, A. M., and Lohrenz, S. E.: Antimony and arsenic biogeochemistry in the western Atlantic Ocean, Deep Sea Research Part II: Topical Studies in Oceanography, 48, 2895-2915, 2001.
De Lange, G. J., Thomson, J., Reitz, A., Slomp, C. P., Speranza Principato, M., Erba, E., and Corselli, C.: Synchronous basin-wide formation and redox-controlled preservation of a Mediterranean sapropel, Nature Geosci, 1, 606-610, 2008.
De Rijk, S., Hayes, A., and Rohling, E. J.: Eastern Mediterranean sapropel S1 interruption: an expression of the onset of climatic deterioration around 7 ka BP, Marine Geology, 153, 337-343, 1999.
deMenocal, P., Ortiz, J., Guilderson, T., Adkins, J., Sarnthein, M., Baker, L., and Yarusinsky, M.: Abrupt onset and termination of the African Humid Period: rapid climate responses to gradual insolation forcing, Quat. Sci. Rev., 19, 347-361, 2000.
Emeis, K.-C., Struck, U., Schulz, H.-M., Rosenberg, R., Bernasconi, S., Erlenkeuser, H., Sakamoto, T., and Martinez-Ruiz, F.: Temperature and salinity variations of Mediterranean Sea surface waters over the last 16,000 years from records of planktonic stable oxygen isotopes and alkenone unsaturation ratios, Palaeogeography, Palaeoclimatology, Palaeoecology, 158, 259-280, 2000.
Emeis, K. C., Schulz, H., Struck, U., Rossignol-Strick, M., Erlenkeuser, H., Howell, M. W., Kroon, D., Mackensen, A., Ishizuka, S., Oba, T., Sakamoto, T., and Koizumi, I.: Eastern Mediterranean surface water temperatures and $\delta^{18}O$ composition during deposition of sapropels in the late Quaternary, Paleoceanography, 18, 1005, 2003.
Essallami, L., Sicre, M. A., Kallel, N., Labeyrie, L., and Siani, G.: Hydrological changes in the Mediterranean Sea over the last 30,000 years, Geochem. Geophys. Geosyst., 8, Q07002, 2007.
Fontugne, M. R. and Calvert, S. E.: Late Pleistocene Variability of the Carbon Isotopic Composition of Organic Matter in the Eastern Mediterranean: Monitor of Changes in Carbon Sources and Atmospheric CO_2 Concentrations, Paleoceanography, 7, 1-20, 1992.
Grelaud, M., Marino, G., Ziveri, P., and Rohling, E. J.: Abrupt shoaling of the nutricline in response to massive freshwater flooding at the onset of the last interglacial sapropel event, Paleoceanography, 27, PA3208, 2012.
Grimm, R.: Simulating the early Holocene eastern Mediterranean sapropel formation using an ocean biogeochemical model, PhD thesis, International Max Planck Research School on Earth System Modelling, Max Planck Institute, Hamburg, 2012.
Hartnett, H. E., Keil, R. G., Hedges, J. I., and Devol, A. H.: Influence of oxygen exposure time on organic carbon preservation in continental margin sediments, Nature, 391, 572-575, 1998.
Hennekam, R., Jilbert, T., Schnetger, B., and de Lange, G. J.: Solar forcing of Nile discharge and sapropel S1 formation in the early to middle Holocene eastern Mediterranean, Paleoceanography, 29, 2013PA002553, 2014.
Herut, B., Almogi-Labin, A., Jannink, N., and Gertman, I.: The seasonal dynamics of nutrient and chlorophyll a concentrations on the SE Mediterranean shelf-slope, Oceanologica Acta, 23, 771-782, 2000.
Jorissen, F. J., de Stigter, H. C., and Widmark, J. G. V.: A conceptual model explaining benthic foraminiferal microhabitats, Marine Micropaleontology, 26, 3-15, 1995.

699 Jorissen, F. J.: Benthic foraminiferal successions across Late Quaternary Mediterranean
700 sapropels, Marine Geology, 153, 91-101, 1999.
701 Kallel, N., Paterne, M., Duplessy, J. C., Vergnaud-Grazzini, C., Pujol, C., Labeyrie, L. D.,
702 Arnold, M., Fontugne, M. R., and Pierre, C.: Enhanced rainfall in the Mediterranean
703 region during the last sapropel event, Oceanol. Acta, 20, 697-712, 1997.
704 Klinkhammer, G. P. and Palmer, M. R.: Uranium in the oceans: Where it goes and why,
705 Geochimica Et Cosmochimica Acta, 55, 1799-1806, 1991.
706 Kotthoff, U., Pross, J., Müller, U. C., Peyron, O., Schmiedl, G., Schulz, H., and Bordon, A.:
707 Climate dynamics in the borderlands of the Aegean Sea during formation of sapropel
708 S1 deduced from a marine pollen record, Quat. Sci. Rev., 27, 832-845, 2008.
709 Krom, M. D., Michard, A., Cliff, R. A., and Strohle, K.: Sources of sediment to the Ionian Sea
710 and western Levantine basin of the Eastern Mediterranean during S-1 sapropel
711 times, Marine Geology, 160, 45-61, 1999.
712 Kuhnt, T., Schmiedl, G., Ehrmann, W., Hamann, Y., and Hemleben, C.: Deep-sea ecosystem
713 variability of the Aegean Sea during the past 22 kyr as revealed by Benthic
714 Foraminifera, Marine Micropaleontology, 64, 141-162, 2007.
715 Kutzbach, J. E., Chen, G., Cheng, H., Edwards, R. L., and Liu, Z.: Potential role of winter
716 rainfall in explaining increased moisture in the Mediterranean and Middle East
717 during periods of maximum orbitally-forced insolation seasonality, Clim. Dyn., 42,
718 1079-1095, 2014.
719 Large, R. R., Halpin, J. A., Danyushevsky, L. V., Maslennikov, V. V., Bull, S. W., Long, J. A.,
720 Gregory, D. D., Lounejeva, E., Lyons, T. W., Sack, P. J., McGoldrick, P. J., and Calver, C.
721 R.: Trace element content of sedimentary pyrite as a new proxy for deep-time
722 ocean–atmosphere evolution, Earth and Planetary Science Letters, 389, 209-220,
723 2014.
724 Laskar, J., Robutel, P., Joutel, F., Gastineau, M., Correia, A. C. M., and Levrard, B.: A long-
725 term numerical solution for the insolation quantities of the Earth, Astron. Astrophys,
726 428, 261–285, 2004.
727 Locarnini, R. A., Mishonov, A. V., Antonov, J. I., Boyer, T. P., Garcia, H. E., Baranova, O. K.,
728 Zweng, M. M., and Johnson, D. R.: World Ocean Atlas 2009, Volume 1: Temperature.
729 In: NOAA Atlas NESDIS 68, Levitus, S. (Ed.), U.S. Government Printing Office,
730 Washington, D.C., 2010.
731 Magny, M., Combourieu-Nebout, N., de Beaulieu, J. L., Bout-Roumazeilles, V., Colombaroli,
732 D., Desprat, S., Francke, A., Joannin, S., Ortu, E., Peyron, O., Revel, M., Sadori, L., Siani,
733 G., Sicre, M. A., Samartin, S., Simonneau, A., Tinner, W., Vannière, B., Wagner, B.,
734 Zanchetta, G., Anselmetti, F., Brugiapaglia, E., Chapron, E., Debret, M., Desmet, M.,
735 Didier, J., Essallami, L., Galop, D., Gilli, A., Haas, J. N., Kallel, N., Millet, L., Stock, A.,
736 Turon, J. L., and Wirth, S.: North-south palaeohydrological contrasts in the central
737 Mediterranean during the Holocene: tentative synthesis and working hypotheses,
738 Clim. Past, 9, 2043-2071, 2013.
739 Marino, G., Rohling, E. J., Sangiorgi, F., Hayes, A., Casford, J. L., Lotter, A. F., Kucera, M., and
740 Brinkhuis, H.: Early and middle Holocene in the Aegean Sea: interplay between high
741 and low latitude climate variability, Quat. Sci. Rev., 28, 3246-3262, 2009.
742 Mayewski, P. A., Meeker, L. D., Twickler, M. S., Whitlow, S., Yang, Q., Lyons, W. B., and
743 Prentice, M.: Major features and forcing of high-latitude northern hemisphere
744 atmospheric circulation using a 110,000-year-long glaciochemical series, Journal of
745 Geophysical Research: Oceans, 102, 26345-26366, 1997.
746 McLennan, S. M.: Relationships between the trace element composition of sedimentary
747 rocks and upper continental crust, Geochem. Geophys. Geosyst., 2, 2001.

748 Meijer, P. T. and Tuenter, E.: The effect of precession-induced changes in the
749 Mediterranean freshwater budget on circulation at shallow and intermediate depth,
750 J. MARINE SYST., 68, 349-365, 2007.
751 Moodley, L., Middelburg, J. J., Herman, P. M. J., Soetaert, K., and de Lange, G. J.:
752 Oxygenation and organic-matter preservation in marine sediments: Direct
753 experimental evidence from ancient organic carbon–rich deposits, Geology, 33, 889-
754 892, 2005.
755 Myers, P. G., Haines, K., and Rohling, E. J.: Modeling the paleocirculation of the
756 Mediterranean: The Last Glacial Maximum and the Holocene with emphasis on the
757 formation of sapropel S1, Paleoceanography, 13, 586-606, 1998.
758 Myers, P. G. and Rohling, E. J.: Modelling a 200-yr interruption of the Holocene Sapropel
759 S_1, Quaternary Res., 53, 98-104, 2000.
760 Nameroff, T. J., Balistrieri, L. S., and Murray, J. W.: Suboxic trace metal geochemistry in
761 the eastern tropical North Pacific, Geochim. Cosmochim. Acta, 66 (7), 1139-1158,
762 2002.
763 Passier, H. F., Middelburg, J. J., van Os, B. J. H., and de Lange, G. J.: Diagenetic pyritisation
764 under eastern Mediterranean sapropels caused by downward sulphide diffusion,
765 Geochimica et Cosmochimica Acta, 60, 751-763, 1996.
766 Pierre, C.: The oxygen and carbon isotope distribution in the Mediterranean water
767 masses, Marine Geology, 153, 41-55, 1999.
768 Pinardi, N. and Masetti, E.: Variability of the large scale general circulation of the
769 Mediterranean Sea from observations and modelling: a review, Palaeogeography,
770 Palaeoclimatology, Palaoecology, 158, 153-173, 2000.
771 Pross, J., Kotthoff, U., Müller, U. C., Peyron, O., Dormoy, I., Schmiedl, G., Kalaitzidis, S., and
772 Smith, A. M.: Massive perturbation in terrestrial ecosystems of the Eastern
773 Mediterranean region associated with the 8.2 kyr B.P. climatic event, Geology, 37,
774 887-890, 2009.
775 Reimer, P. J., Bard, E., Bayliss, A., Beck, J. W., Blackwell, P. G., Bronk Ramsey, C., Buck, C.
776 E., Cheng, H., Edwards, R. L., Friedrich, M., Grootes, P. M., Guilderson, T. P.,
777 Haflidason, H., Hajdas, I., Hatté, C., Heaton, T. J., Hoffmann, D. L., Hogg, A. G., Hughen,
778 K. A., Kaiser, K. F., Kromer, B., Manning, S. W., Niu, M., Reimer, R. W., Richards, D. A.,
779 Scott, E. M., Southon, J. R., Staff, R. A., Turney, C. S. M., and van der Plicht, J.: IntCal13
780 and Marine13 Radiocarbon Age Calibration Curves 0–50,000 Years cal BP, 2013,
781 2013. 2013.
782 Reitz, A., Thomson, J., de Lange, G. J., and Hensen, C.: Source and development of large
783 manganese enrichments above eastern Mediterranean sapropel S1,
784 Paleoceanography, 21, PA3007, 2006.
785 Renssen, H., Brovkin, V., Fichefet, T., and Goosse, H.: Simulation of the Holocene climate
786 evolution in Northern Africa: The termination of the African Humid Period, Quatern.
787 Int., 150, 95-102, 2006.
788 Revel, M., Colin, C., Bernasconi, S., Combourieu-Nebout, N., Ducassou, E., Grousset, F.,
789 Rolland, Y., Migeon, S., Bosch, D., Brunet, P., Zhao, Y., and Mascle, J.: 21,000 Years of
790 Ethiopian African monsoon variability recorded in sediments of the western Nile
791 deep-sea fan, Reg Environ Change, doi: 10.1007/s10113-014-0588-x, 2014. 1-12,
792 2014.
793 Revel, M., Ducassou, E., Grousset, F. E., Bernasconi, S. M., Migeon, S., Revillon, S., Mascle,
794 J., Murat, A., Zaragosi, S., and Bosch, D.: 100,000 Years of African monsoon variability
795 recorded in sediments of the Nile margin, Quat. Sci. Rev., 29, 1342-1362, 2010.

796 Roether, W., Manca, B. B., Klein, B., Bregant, D., Georgopoulos, D., Beitzei, V., Kovacevic,
797 V., and Luchetta, A.: Recent changes in Eastern Mediterranean Deep Waters, Science,
798 271, 333-335, 1996.
799 Rohling, E., Mayewski, P., Abu-Zied, R., Casford, J., and Hayes, A.: Holocene atmosphere-
800 ocean interactions: records from Greenland and the Aegean Sea, Clim. Dyn., 18, 587-
801 593, 2002.
802 Rohling, E. J.: Review and new aspects concerning the formation of eastern
803 Mediterranean sapropels, Marine Geology, 122, 1-28, 1994.
804 Rohling, E. J., Jorissen, F. J., and De Stigter, H. C.: 200 Year interruption of Holocene
805 sapropel formation in the Adriatic Sea, Journal of Micropalaeontology, 16, 97-108,
806 1997.
807 Rohling, E. J., Marino, G., and Grant, K. M.: Mediterranean climate and oceanography, and
808 the periodic development of anoxic events (sapropels), Earth-Science Reviews, 143, 62-
809 97, 2015.
810 Rossignol-Strick, M., Nesteroff, W., Olive, P., and Vergnaud-Grazzinni, C.: After the
811 deluge: Mediterranean stagnation and sapropel formation, Nature, 295, 105-110,
812 1982.
813 Schlitzer, R.: Ocean data view. http://odv.awi.de. (Ed.), 2009.
814 Schmiedl, G., Kuhnt, T., Ehrmann, W., Emeis, K.-C., Hamann, Y., Kotthoff, U., Dulski, P., and
815 Pross, J.: Climatic forcing of eastern Mediterranean deep-water formation and
816 benthic ecosystems during the past 22 000 years, Quat. Sci. Rev., 29, 3006-3020,
817 2010.
818 Shimmield, G. B. and Price, N. B.: The behaviour of molybdenum and manganese during
819 early sediment diagenesis — offshore Baja California, Mexico, Marine Chemistry, 19,
820 261-280, 1986.
821 Siani, G., Magny, M., Paterne, M., Debret, M., and Fontugne, M.: Paleohydrology
822 reconstruction and Holocene climate variability in the South Adriatic Sea, Clim. Past,
823 9, 499-515, 2013.
824 Siani, G., Paterne, M., Arnold, M., Bard, E., Mativier, B., Tisnerat, N., and Bassinot, F.:
825 Radiocarbon Reservoir Ages In The Mediterranean Sea And Black Sea, Radiocarbon,
826 42, 271-280, 2000.
827 Siani, G., Paterne, M., Michel, E., Sulpizio, R., Sbrana, A., Arnold, M., and Haddad, G.:
828 Mediterranean Sea Surface Radiocarbon Reservoir Age Changes Since the Last
829 Glacial Maximum, Science, 294, 1917-1920, 2001.
830 Soulet, G., Menot, G., Lericolais, G., and Bard, E.: A revised calendar age for the last
831 reconnection of the Black Sea to the global ocean, Quat. Sci. Rev., 30, 1019-1026,
832 2011.
833 Stratford, K., Williams, R. G., and Myers, P. G.: Impact of the circulation on Sapropel
834 Formation in the eastern Mediterranean, Global Biogeochem. Cycles, 14, 683-695,
835 2000.
836 Stuiver, M. and Reimer, P. J.: CALIB Radiocarbon Calibration program, available online at
837 http://calib.qub.ac.uk/calib/. 1986-2013.
838 Thomson, J., Higgs, N. C., Wilson, T. R. S., Croudace, I. W., De Lange, G. J., and Van
839 Santvoort, P. J. M.: Redistribution and geochemical behaviour of redox-sensitive
840 elements around S1, the most recent eastern Mediterranean sapropel, Geochimica et
841 Cosmochimica Acta, 59, 3487-3501, 1995.
842 Thomson, J., Mercone, D., De Lange, G. J., and Van Santvoort, P. J. M.: Review of recent
843 advances in the interpretation of eastern Mediterranean sapropel S1 from
844 geochemical evidence, Marine Geology, 153, 77-89, 1999.

Tjallingii, R., Röhl, U., Kolling, M., and Bickert, T.: Influence of the water content on X-ray fluorescence core-scanning measurements in soft marine sediments, Geochem. Geophys. Geosyst., 8, Q02004, 2007.

Tomczak, M. and Godfrey, J. S.: Regional oceanography: an introduction, Elsevier, Oxford, 1994.

Tribovillard, N., Algeo, T. J., Lyons, T., and Riboulleau, A.: Trace metals as paleoredox and paleoproductivity proxies: An update, Chem. Geol., 232, 12-32, 2006.

van Santvoort, P. J. M., de Lange, G. J., Thomson, J., Cussen, H., Wilson, T. R. S., Krom, M. D., and Ströhle, K.: Active post-depositional oxidation of the most recent sapropel (S1) in sediments of the eastern Mediterranean Sea, Geochimica et Cosmochimica Acta, 60, 4007-4024, 1996.

Vidal, L., Menot, G., Joly, C., Bruneton, H., Rostek, F., Cagatay, M. N., Major, C., and Bard, E.: Hydrology in the Sea of Marmara during the last 23 ka: Implications for timing of Black Sea connections and sapropel deposition, Paleoceanography, 25, PA1205, 2010.

Waelbroeck, C., Labeyrie, L., Michel, E., Duplessy, J.-C., McManus, J. F., Lambeck, K., Balbon, E., and Labrancherie, M.: Sea-level and deep water temperature changes derived from benthic foraminifera isotopic records, Quat. Sci. Rev., 21, 295–305, 2002.

Wehausen, R. and Brumsack, H.-J.: Chemical cycles in Pliocene sapropel-bearing and sapropel-barren eastern Mediterranean sediments, Palaeogeography, Palaeoclimatology, Palaeoecology, 158, 325-352, 2000.

Weldeab, S., Menke, V., and Schmiedl, G.: The pace of East African monsoon evolution during the Holocene, Geophysical Research Letters, 41, 2014GL059361, 2014.

Ziegler, M., Jilbert, T., de Lange, G. J., Lourens, L. J., and Reichart, G.-J.: Bromine counts from XRF scanning as an estimate of the marine organic carbon content of sediment cores, Geochem. Geophys. Geosyst., 9, Q05009, 2008.

Ziegler, M., Tuenter, E., and Lourens, L. J.: The precession phase of the boreal summer monsoon as viewed from the eastern Mediterranean (ODP Site 968), Quat. Sci. Rev., 29, 1481-1490, 2010.

875 Table 1. Radiocarbon ages for core MD04-2722

Depth in core (cm)	AMS sample nº	^{14}C age ± 1σ (yr BP)	Cal. age* (yr BP)	95.4 % (2σ) cal age ranges (yr BP)
2	SacA26352	3765 ± 30	3700	3604 - 3812
20	SacA26353	4400 ± 30	4551	4433 - 4678
48	SacA31590	5760 ± 40	6188	6061 - 6277
64	SacA26354	6790 ± 30	7318	7249 - 7396
80	SacA31591	7485 ± 45	7945	7835 - 8042
112	SacA26355	8980 ± 35	9629	9525 - 9763
136	SacA26356	10680 ± 40	12048	11843 - 12292
150	SacA26357	11925 ± 40	13377	13275 - 13483
176	SacA26358	13675 ± 45	15955	15762 - 16130
192	SacA26359	15170 ± 50	17964	17793 - 18139
220	SacA26360	18030 ± 60	21313	21040 - 21555
250	SacA26361	20000 ± 70	23611	23354 - 23878

876 * Median probability

877

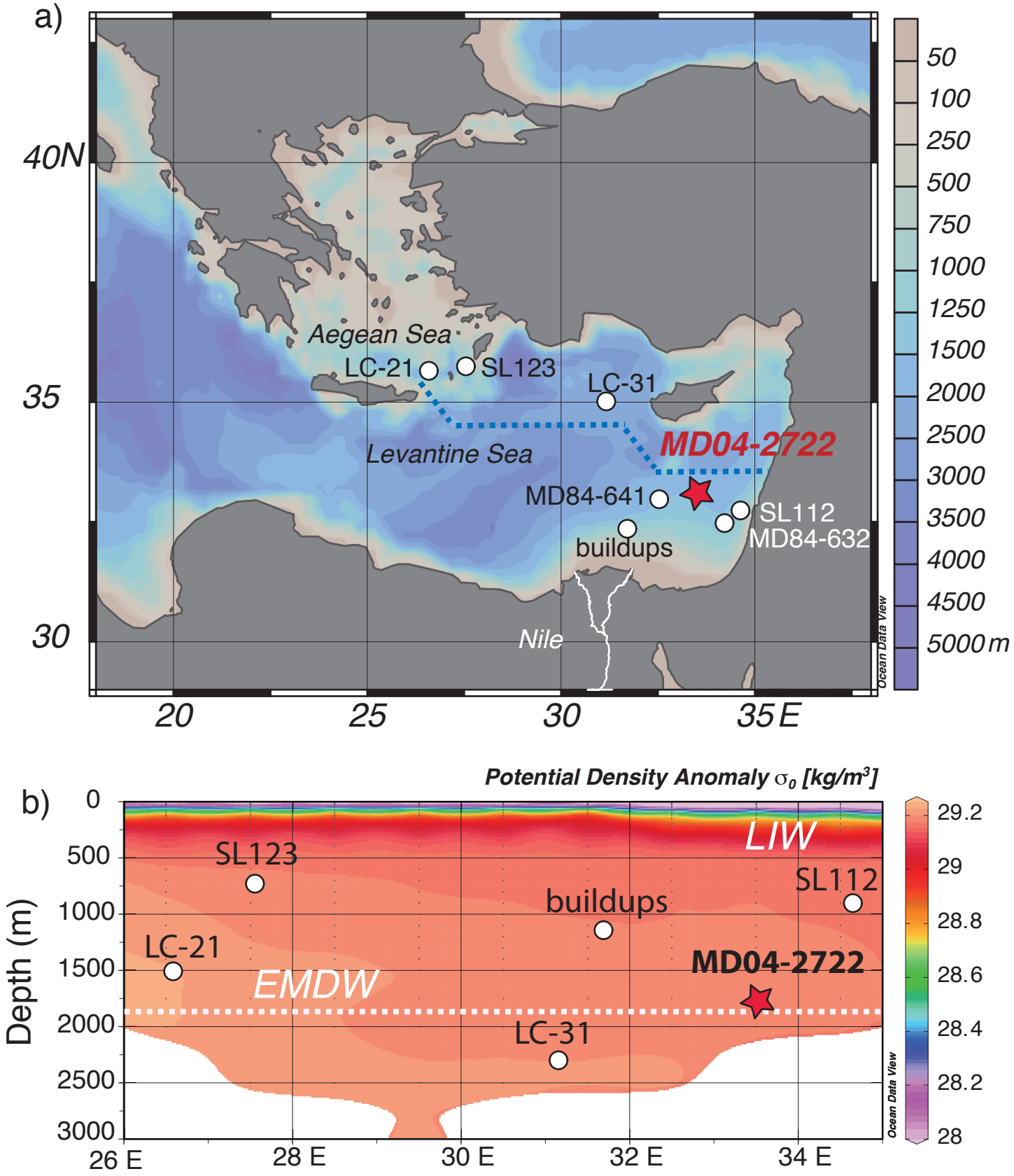
a)
40N
35
30
20
25
30
35 E
Aegean Sea
LC-21
SL123
LC-31
Levantine Sea
MD04-2722
MD84-641
SL112
MD84-632
buildups
Nile
Ocean Data View
50
100
250
500
750
1000
1250
1500
2000
2500
3000
3500
4000
4500
5000 m
b)
Potential Density Anomaly σ0 [kg/m³]
Depth (m)
0
500
1000
1500
2000
2500
3000
26 E
28 E
30 E
32 E
34 E
SL123
LC-21
EMDW
LIW
buildups
SL112
MD04-2722
LC-31
Ocean Data View
29.2
29
28.8
28.6
28.4
28.2
28

Figure 1

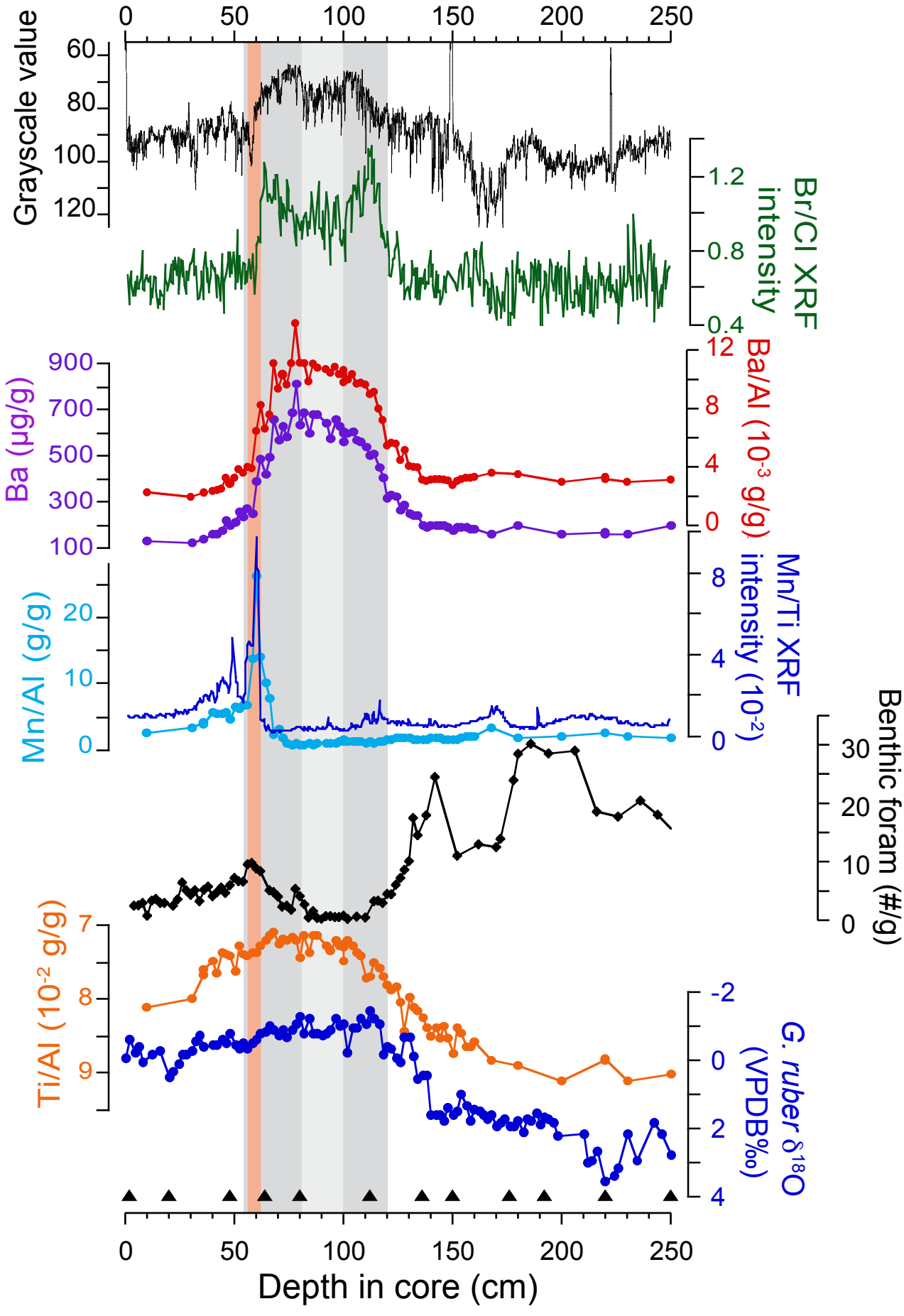
Grayscale value
Br/Cl XRF intensity
Ba (µg/g)
Ba/Al (10-3 g/g)
Mn/Al (g/g)
Mn/Ti XRF intensity (10-2)
Benthic foram (#/g)
Ti/Al (10-2 g/g)
G. ruber δ18O (VPDB‰)
Depth in core (cm)

Figure 2

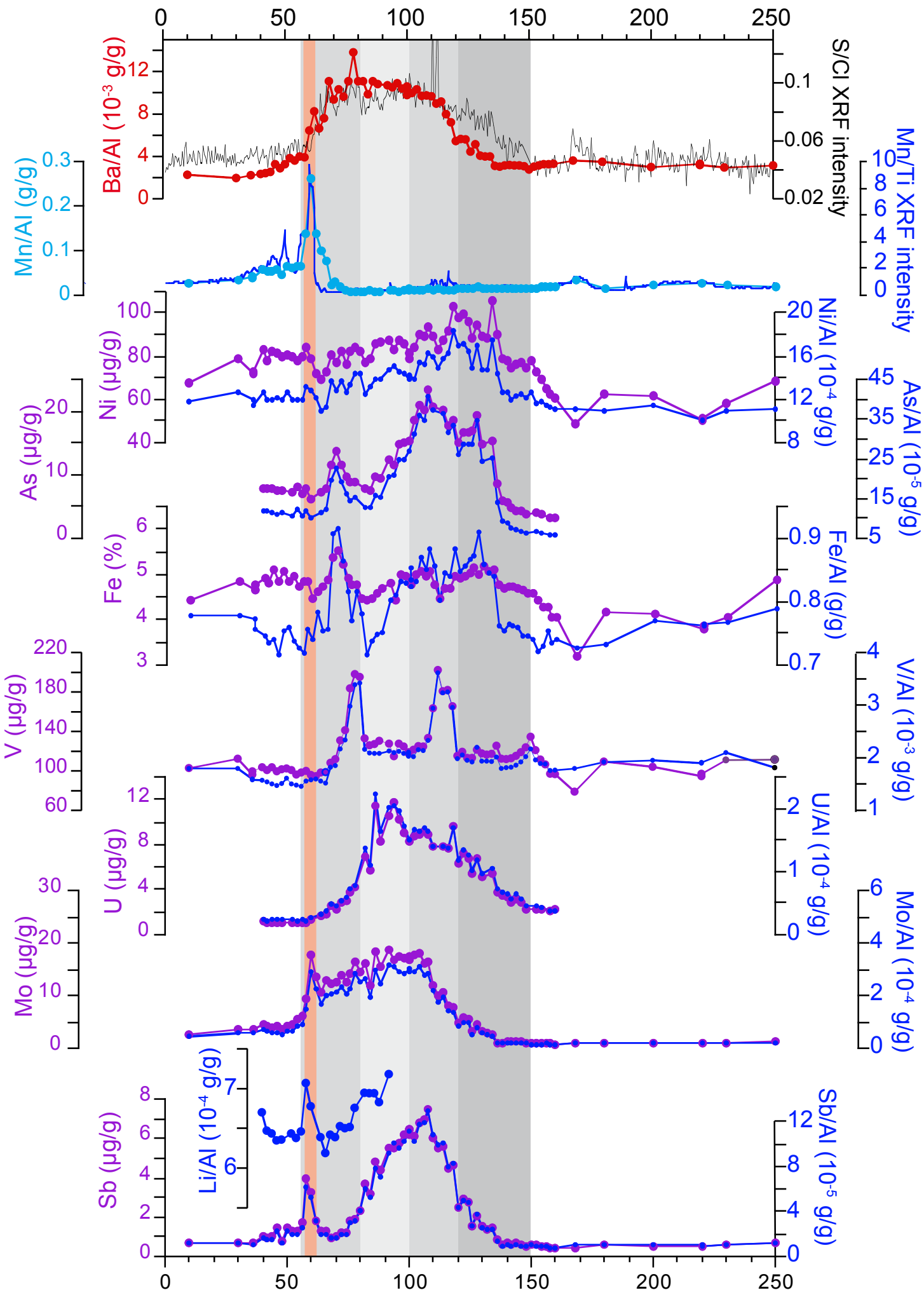
Ba/Al (10-3 g/g)
S/Cl XRF intensity
Mn/Al (g/g)
Mn/Ti XRF intensity
Ni (µg/g)
Ni/Al (10-4 g/g)
As (µg/g)
As/Al (10-5 g/g)
Fe (%)
Fe/Al (g/g)
V (µg/g)
V/Al (10-3 g/g)
U (µg/g)
U/Al (10-4 g/g)
Mo (µg/g)
Mo/Al (10-4 g/g)
Li/Al (10-4 g/g)
Sb (µg/g)
Sb/Al (10-5 g/g)
Depth in core (cm)

Figure 3

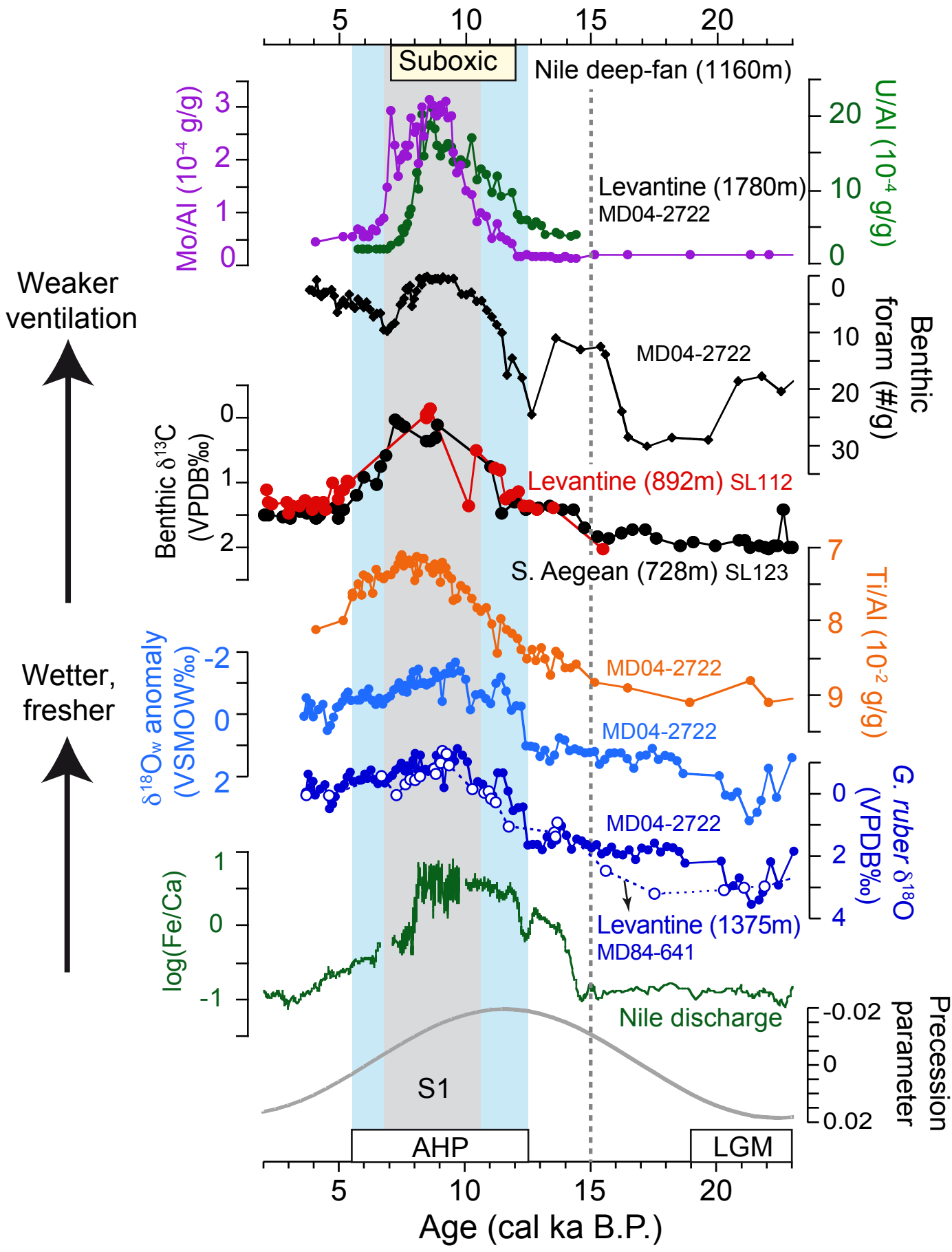
Suboxic
Nile deep-fan (1160m)
Mo/Al (10⁻⁴ g/g)
U/Al (10⁻⁴ g/g)
Levantine (1780m)
MD04-2722
Weaker ventilation
Benthic foram (#/g)
MD04-2722
Benthic δ¹³C (VPDB‰)
Levantine (892m) SL112
S. Aegean (728m) SL123
Ti/Al (10⁻² g/g)
MD04-2722
Wetter, fresher
δ¹⁸Ow anomaly (VSMOW‰)
MD04-2722
MD04-2722
G. ruber δ¹⁸O (VPDB‰)
Levantine (1375m)
MD84-641
log(Fe/Ca)
Nile discharge
S1
Precession parameter
AHP
LGM
Age (cal ka B.P.)

Figure 4

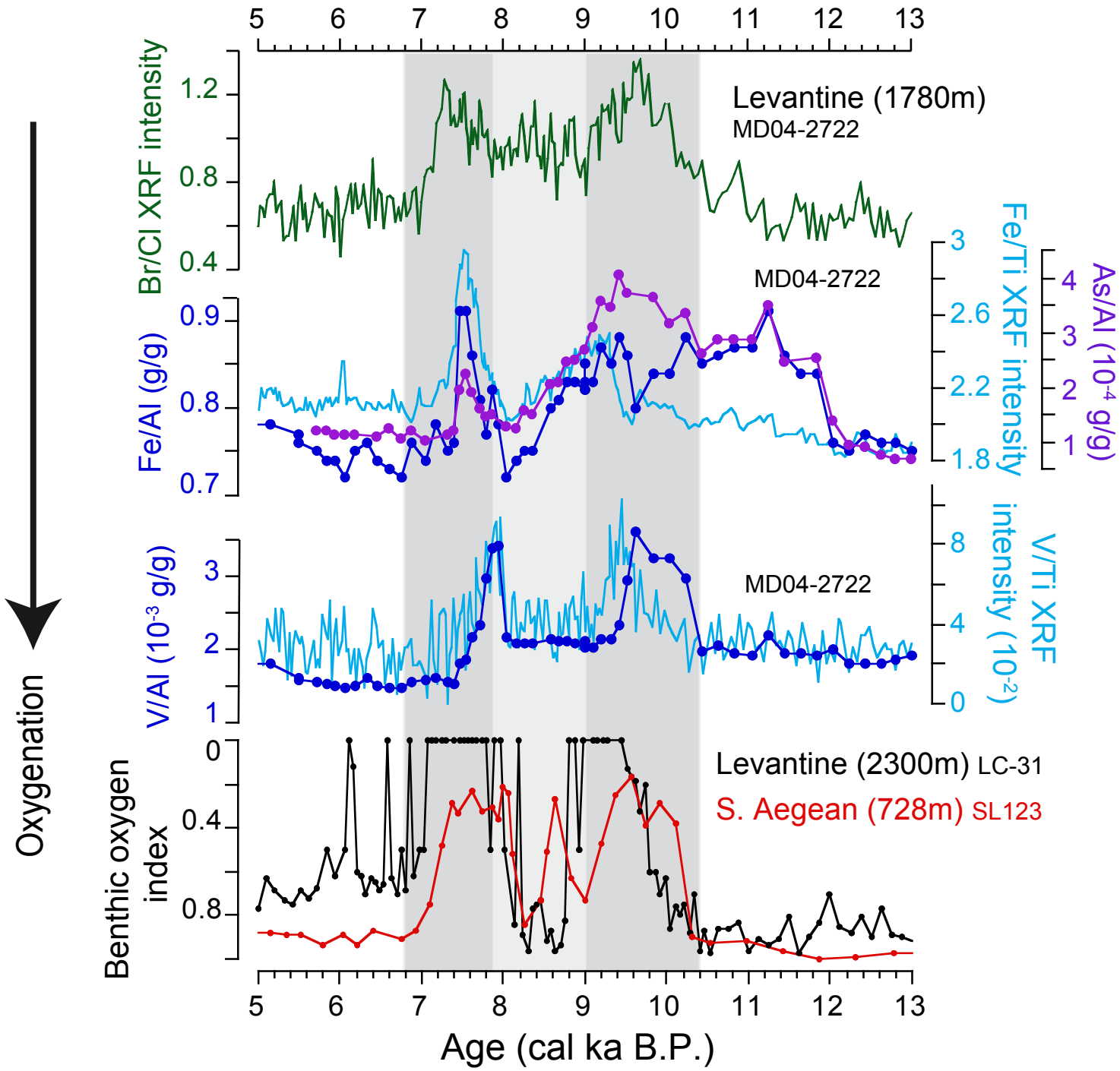
Oxygenation
Br/Cl XRF intensity
Levantine (1780m)
MD04-2722
Fe/Al (g/g)
MD04-2722
Fe/Ti XRF intensity
As/Al (10-4 g/g)
V/Al (10-3 g/g)
MD04-2722
V/Ti XRF intensity (10-2)
Benthic oxygen index
Levantine (2300m) LC-31
S. Aegean (728m) SL123
Age (cal ka B.P.)

Figure 5

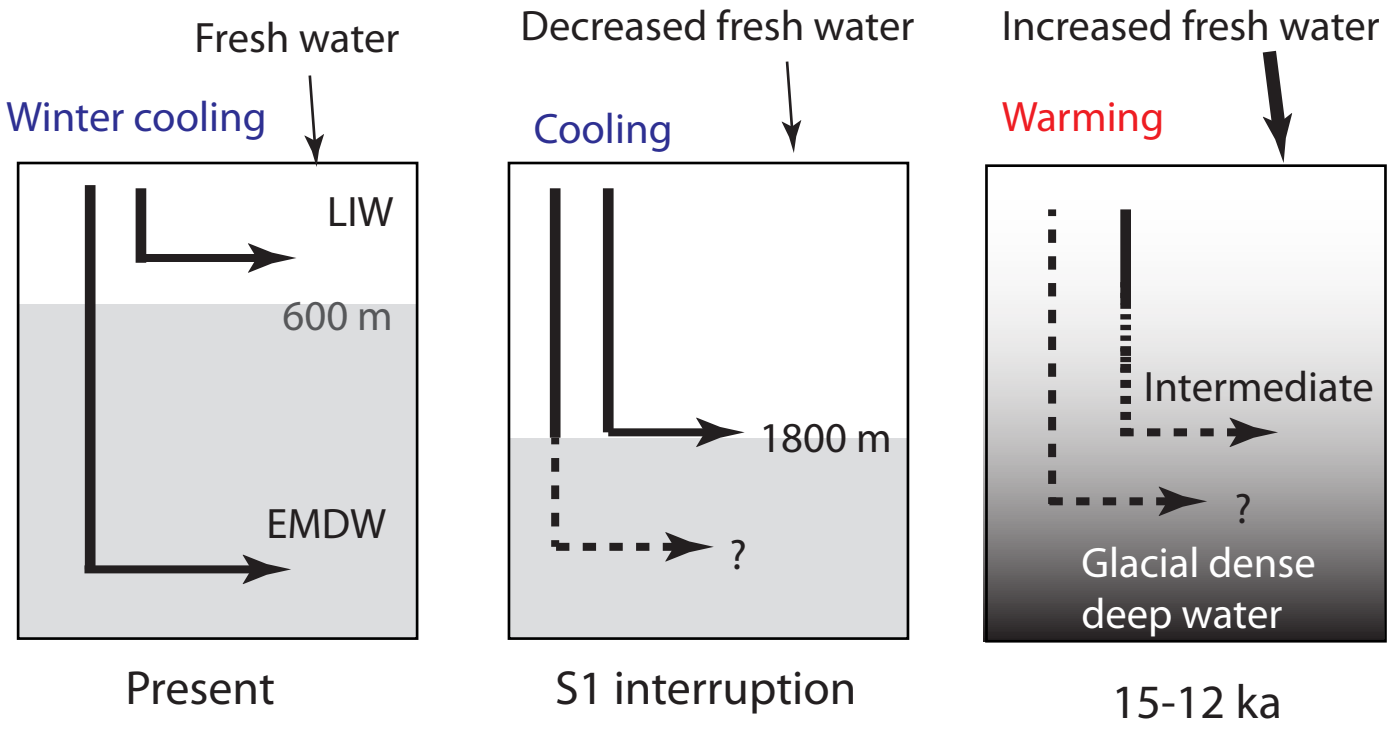
Fresh water
Winter cooling
LIW
600 m
EMDW
Present
Decreased fresh water
Cooling
1800 m
?
S1 interruption
Increased fresh water
Warming
Intermediate
?
Glacial dense
deep water
15-12 ka

Figure 6